

Stripe-like nanoscale structural phase separation and optimal inhomogeneity in superconducting $\text{BaPb}_{1-x}\text{Bi}_x\text{O}_3$

P. Giraldo-Gallo,^{1,2} Y. Zhang,^{3,4} C. Parra,^{1,2,5,6} H. C. Manoharan,^{1,2,5}
M. R. Beasley,^{1,7} T. H. Geballe,^{1,7} M. J. Kramer,³ and I. R. Fisher^{1,7}

¹*Geballe Laboratory for Advanced Materials, Stanford University, Stanford, CA 94305, USA*

²*Department of Physics, Stanford University, CA 94305, USA*

³*Ames Laboratory (USDOE), Department of Materials Science and Engineering, Iowa State University, Ames IA 50011-3020, USA*

⁴*Beijing National Laboratory for Condensed Matter Physics, Institute of Physics, Chinese Academy of Sciences, Beijing 100190, China*

⁵*Stanford Institute for Materials and Energy Sciences, SLAC National Accelerator Laboratory, Menlo Park, CA 94025, USA*

⁶*Departamento de Física, Universidad Técnica Federico Santa María, Valparaíso, Chile*

⁷*Department of Applied Physics, Stanford University, CA 94305, USA*

(Dated: August 22, 2018)

Structural phase separation in the form of partially disordered stripes, with characteristic length scales in the nanometer range, is observed for superconducting $\text{BaPb}_{1-x}\text{Bi}_x\text{O}_3$. The evolution of the superconducting coherence length with composition relative to the size of these stripes suggests an important role of the nanostructure in determining the shape of the superconducting dome. It is proposed that the maximum T_c is determined by a kind of “optimal inhomogeneity”, characterized by a crossover from an inhomogeneous macroscopic superconductor to a granular superconductor for which phase fluctuations suppress T_c .

High temperature superconductors (HTSCs) are complex materials with many degrees of freedom, including spin, charge, orbital and structural. Spontaneous segregation of electronic phases potentially plays an important role in defining several important physical properties in these materials, including the critical temperature T_c . Phase separation in the charge channel has been observed in underdoped cuprates in the form of stripes [1, 2], and recently, in the form of charge density wave (CDW) nano-domains [3]. Details of the nanostructure associated with this phase separation, and its connection with the optimization of T_c in these systems is an important open question [4–6]. For systems with such a variety of interactions, tracking the influence of each individual degree of freedom on the phase separation and on the determination of the electronic properties is challenging. For this reason, the study of simpler superconducting systems can provide useful insights for understanding more complex materials. A model system for the study of how superconductivity is influenced by local CDW instabilities and structural phase separation can be found in the bismuthate superconductors.

The family of bismuthate superconductors results from replacing K for Ba, or Pb for Bi, in BaBiO_3 , a charge density wave (CDW) insulator [8–11]. This family of superconductors has no magnetic degrees of freedom. Upon doping, the insulating CDW phase disappears, giving rise to a metallic phase where superconductivity appears at (maximum) temperatures below 30K and 11K for K-doping and Pb-doping, respectively [12, 13]. Structural phase separation on a nanoscopic scale has been observed in $\text{BaPb}_{1-x}\text{Bi}_x\text{O}_3$ for superconducting compo-

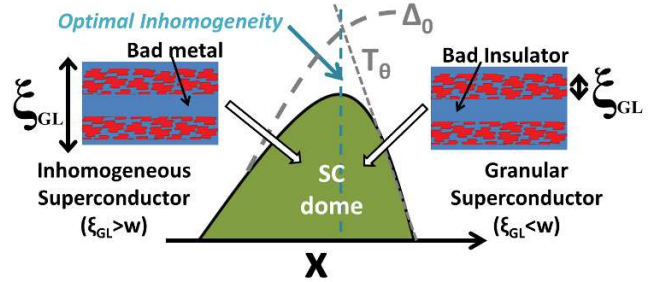


FIG. 1: (Color online) Stylized cartoon illustrating the effect of the competing length scales associated with structural phase separation and the superconducting coherence length on the superconducting phase diagram of $\text{BaPb}_{1-x}\text{Bi}_x\text{O}_3$ (see discussion in main text). Red and blue regions correspond to tetragonal and orthorhombic polymorphs respectively. The pairing interaction is understood to originate in the tetragonal material [7].

sitions [14], but the implications in shaping the superconducting dome, in particular close to the disorder induced metal-insulator transition at $x = 0.30$ [15] followed closely by the opening of a gap in the optical spectrum at $x \approx 0.35$, remain an open question. In this letter we report the observation of stripe-like structural phase separation in superconducting $\text{BaPb}_{1-x}\text{Bi}_x\text{O}_3$ for compositions spanning optimal doping. Remarkably, the maximum T_c occurs when the superconducting coherence length matches the size of the partially disordered stripes, implying a connection between the structural phase sep-

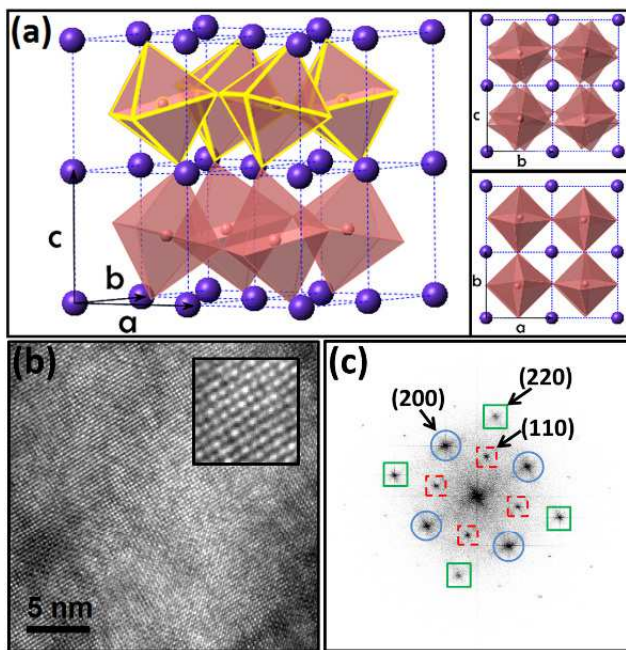


FIG. 2: (Color online) (a) Schematic diagram illustrating the $a^0b^-b^-$ distortion of the cubic perovskite structure, resulting in a orthorhombic $Ibmm$ unit cell. The rotations of the octahedra have been exaggerated in the illustrations to more clearly reveal the distortion. (b) HRTEM image for a sample with $x=0.18$, looking down the $[001]$ zone axis, revealing a well-ordered structure with coherent planes of atoms. Inset shows an expanded view of a region of $3 \times 3 \text{ nm}^2$. (c) FFT of the image in fig. 2(b), showing peaks corresponding to the $[200]$ (blue-solid circles), $[110]$ (red-dashed squares) and $[220]$ (green-solid squares) set of reflections. Symbols with solid edges correspond to reflections allowed in both $Ibmm$ and I_4/mcm space groups, while those with dashed edges correspond to reflections forbidden in the I_4/mcm space group, but allowed in the $Ibmm$.

aration, the enhanced coulomb effects due to disorder (localization), the inhomogeneous superconducting properties, and the shape of the superconducting “dome” (see figure 1).

$\text{BaPb}_{1-x}\text{Bi}_x\text{O}_3$ has a distorted perovskite (ABO_3) crystal structure. For the highest Bi concentrations the material comprises two distinct Bi sites, with different Bi-O bond lengths. The origin of the associated charge density wave (CDW) has been widely debated [9, 16–18]. For $x \leq 0.8$ the average structure comprises a single Bi/Pb site [19], though EXAFS measurements reveal two distinct Bi-O bond lengths down to at least $x \sim 0.25$ [20], implying a persistence of the CDW at a local level. Significantly, for all compositions, the perovskite structure is also distorted by rotational instabilities of the oxygen octahedra, which can be described using Glazer’s notation [21, 22]. For the insulating end-member compound BaBiO_3 ($x = 1$), and down to $x = 0.9$, the unit cell

space group is monoclinic $I2/m$ (coming from a $a^0b^-c^-$ tilt, in Glazer’s notation); for the metallic end-member compound BaPbO_3 ($x = 0$) and up to $x \approx 0.15$, and again for $0.35 < x < 0.9$, the unit cell space group is orthorhombic $Ibmm$ (coming from a $a^0b^-b^-$ tilt, as shown in fig. 2(a)); however, for the region of $0.15 < x < 0.35$, which is also the range of compositions for which the material is superconducting, the material is polymorphic, with a fraction of its volume with orthorhombic $Ibmm$ symmetry and the rest with tetragonal I_4/mcm symmetry (coming from a $a^0a^0c^-$ tilt) [7]. The superconducting volume fraction peaks at the same Bi composition where the tetragonal-to-orthorhombic ratio is maximum, leading to the conclusion that the tetragonal polymorph is the one responsible for superconductivity in this material [7, 19]. This Bi composition is also the one for which the material has the maximum T_c , i.e., the optimal doping composition.

In the interest of investigating how the polymorphism is accommodated microscopically in a “single crystal” of $\text{BaPb}_{1-x}\text{Bi}_x\text{O}_3$, and its possible consequences for the observed transport and, more interestingly, superconducting properties, high-resolution transmission electron microscopy (HRTEM) measurements were taken for samples with bismuth compositions below, at and above optimal doping. Samples of each concentration were crushed in liquid-nitrogen-cooled ethyl alcohol, and the liquid was allowed to warm to room temperature. The slurry was stirred and a small droplet was placed on a holey carbon grid and dried in air. The samples were analyzed using a FEI G2 F20TEM Tecnai STEM operated at 200 keV. Thin areas were analyzed with selected area diffraction, energy dispersive spectroscopy, and high-resolution imaging. Thin areas were aligned with either the $[010]$ or the $[001]$ zone axis based on indexing to the $Ibmm$ structure (space group No. 74), showing clear lattice fringes in the HRTEM. All the HRTEM images taken for all the different compositions reveal a well-ordered structure, as can be observed in the $24.1 \times 24.1 \text{ nm}^2$ image in fig. 2(b) for a sample with Bi composition of $x = 0.18$, and better appreciated in the $3 \times 3 \text{ nm}^2$ expanded view in the inset to this figure. Fig. 2(c) shows its corresponding fast Fourier transform (FFT), revealing peaks from both tetragonal (hkl even) and orthorhombic (hkl even and odd, in the tetragonal notation) phases. In ref. [14] we showed that it is possible to recreate the spatial separation of the two polymorphs by systematically masking these diffraction peaks and performing an inverse Fourier transform (IFFT). In this way, we can obtain information about the length scales associated with the polymorphic variation across a sample.

In order to quantify the length scales associated with the orthorhombic variation, the average spatial correlation function $\langle G(\vec{r}) \rangle$, and the angle-dependent spatial correlation function $\langle G_\theta(\vec{r}) \rangle$ were computed for each $[110]_T/[101]_T$ filtered IFFT image (see supplemental

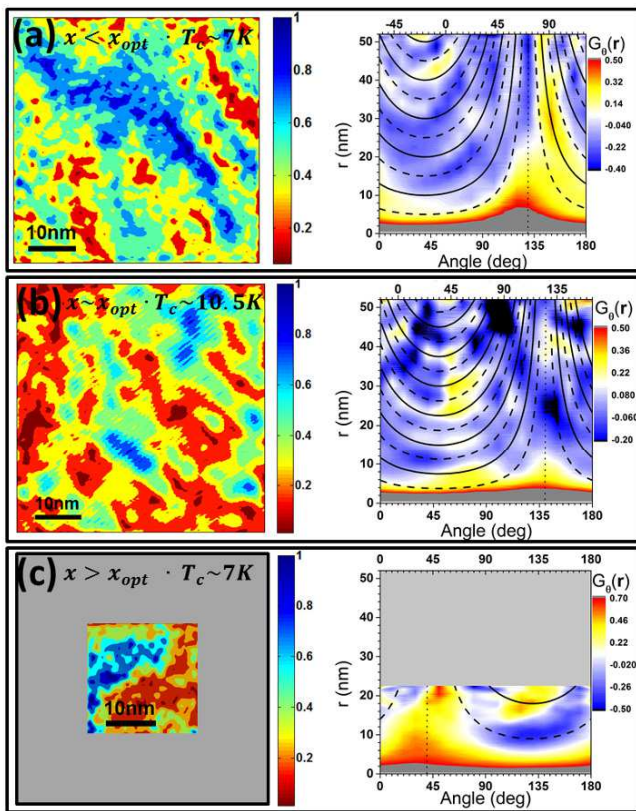


FIG. 3: (Color online) $[110]_T/[101]_T$ filtered-and-reconstructed HRTEM images (after averaging-out the atomic-scale variation), and their respective angle-dependent correlation functions, $\langle G_\theta(\vec{r}) \rangle$, for bismuth compositions of (a) $x=0.18$ (i.e. $x < x_{opt}$, $T_c \approx 7\text{K}$) (b) $x=0.24$ ($x \sim x_{opt}$, $T_c \approx 10.5\text{K}$), and (c) $x=0.28$ ($x > x_{opt}$, $T_c \approx 7\text{K}$). Vertical bars next to each image show the normalized intensity color scale.

Blue regions are more strongly orthorhombic, red regions are less strongly orthorhombic (i.e. more strongly tetragonal). The color scale on the right hand side plots represent the value of $\langle G_\theta(\vec{r}) \rangle$. This quantity is plotted as a function of $|\vec{r}|$ (vertical axis) and the angle θ with the horizontal (bottom-axis) or the $[200]_T$ crystalline axis (top-axis). Solid and dashed lines represent the best fits to $N \times d / \cos((\alpha - 90^\circ) - \theta)$ and $(2N - 1) \times w / \cos((\alpha - 90^\circ) - \theta)$ for the local maxima and minima respectively, as described in the main text.

material for definitions). Fig. 3 shows filtered-and-reconstructed HRTEM images for a representative sample of each Bi composition studied (left panels), after a resolution reduction from 0.47\AA per pixel, to 4.1\AA per pixel, therefore eliminating the atomic resolution information while keeping the longer-range variation in “orthorhombicity” (see supplemental material). Both, $\langle G(\vec{r}) \rangle$ (shown in supplemental material) and $\langle G_\theta(\vec{r}) \rangle$ (shown on the right panels of fig. 3) of all the images shown, reveal local minima and maxima, implying the presence of characteristic length scales for the phase sep-

aration. Furthermore, the angular dependent correlation function $\langle G_\theta(\vec{r}) \rangle$ clearly reveals that there is a particular spatial pattern associated with the phase separation. Inspection of these quantities, in the right-hand panels of figure 3, reveals arcs of intensity with an approximately two-fold rotational symmetry. The arcs are imperfect, but repeat with a fixed periodicity, implying a self-organized pattern of phase separation over remarkably large length scales. Such a pattern of intensity in $\langle G_\theta(\vec{r}) \rangle$ is consistent with a real space phase separation comprising partially disordered stripes (see supplemental material). For a system with stripes separated by a distance d and running along an angle α with respect to the horizontal, the distance between stripes as measured at an angle θ is given by $N \times d / \cos((\alpha - 90^\circ) - \theta)$ (with $N = 1, 2, 3, \dots$), which diverges at $\theta = \alpha$. As can be observed in Fig. 3 (and in similar data shown in the supplemental material), most of the samples studied exhibit this characteristic dependence, with periodic maxima (shown by solid lines in the figure) and minima (dashed lines) that approximately follow such an inverse cosine function. The orientation of the stripes with respect to the crystal axes is not identical for all images studied, but on average it is close to $29^\circ \pm 22^\circ$ from the $[100]_T$ orientation. These stripes are clearly evident in the larger area real space images shown in the left hand panels of Fig. 3(a,b), running approximately top-left to bottom-right. In addition to the separation of stripes, inspection of the images in Fig. 3 reveals that there is a shorter (and more isotropic) length scale of structural variation, which describes the broken-up character of the stripes. This length scale can be seen more clearly in the average correlation function as a kink in the low- r tail, which can be better identified in the derivative of $\langle G(\vec{r}) \rangle$.

Although the stripe-like character of the structural phase separation is imperfect, nevertheless by identifying the morphology of the nanostructure we are able to define the characteristic length scales of phase separation in terms of three simple parameters (see inset to fig. 4): the stripe period, d , (i.e. the distance between stripes of similar “orthorhombicity”, determined from the maxima of $\langle G_\theta(\vec{r}) \rangle$); the stripe width, w (estimated from the regions of minimum values in $\langle G_\theta(\vec{r}) \rangle$, i.e. stripes half-period, which can be used as a measure of the upper bound to the width of individual stripes); and the length scale associated with disorder within a stripe, ζ , (identified in the derivative of the low- r tail of $\langle G(\vec{r}) \rangle$). The analysis described above, was performed for a total of five $x = 0.18$ samples, four $x = 0.24$ samples and four $x = 0.28$ samples (all of which are shown in the supplemental material), and the average value of d , w and ζ for each Bi composition were calculated. The results are summarized in Fig. 4, together with the error obtained by calculating the standard deviation from the average value.

The phase separation of tetragonal and orthorhombic

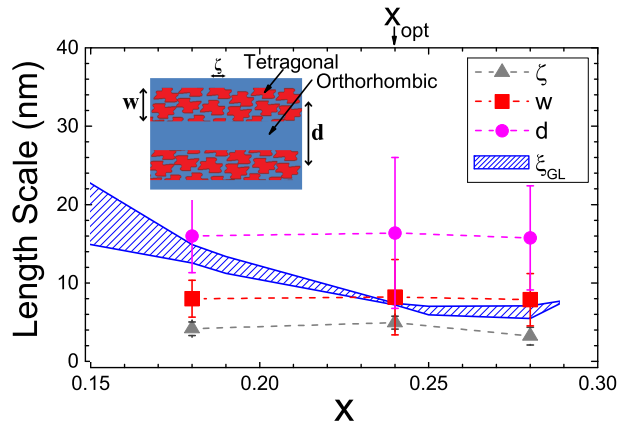


FIG. 4: (Color online) Average characteristic lengths of phase separation for $\text{BaPb}_{1-x}\text{Bi}_x\text{O}_3$ as a function of x .

These data are contrasted with the Ginzburg-Landau coherence length $\xi_{GL}(0)$, represented in the blue curves.

polymorphs is presumably driven by changes in the relative free energy of the two phases, both as a function of temperature and composition. The resulting morphology is reminiscent of spinodal decomposition, but the physical origin is somewhat different in this case, involving two competing phases (see supplemental material). Significantly, in such a scenario, the composition $x_{opt} \sim 0.24$, at which the tetragonal volume fraction is maximal, marks the separatrix between formation of two different orthorhombic phases, both with the same structure, but one with a lower Bi concentration (for compositions $x < x_{opt}$), and one with a higher Bi concentration ($x > x_{opt}$). Since the free energy of each polymorph can be affected by strain [23], local variations in the local strain is anticipated to broaden or smear the otherwise sharp distinction in the variation of Bi composition. Considering the temperature dependence of the resistivity for compositions that have only an orthorhombic structure, it is clear that Bi substitution leads to a progressive evolution of the electronic properties of the orthorhombic phase from a “bad metal” for $x \ll x_{opt}$ (i.e. $d\rho/dT > 0$, but with a very large absolute value of the resistivity) to a “bad insulator” for $x \gg x_{opt}$ (i.e. $d\rho/dT < 0$, but nevertheless extrapolating to a finite conductivity at $T = 0$) [8, 14, 24]. It is unclear whether this evolution of the electronic properties of the orthorhombic phase is driven by disorder due to the increasing Bi concentration, or a progressive increase in the CDW correlation length, or indeed a combination of both effects, but tunneling data clearly indicates that the zero temperature conductivity decreases to zero linearly in the entire range from $x = 0$ to $x = 0.3$, and that the associated zero bias tunneling anomaly also varies smoothly over this range [15]. Of particular significance for the following discussion, if the Bi concentration deviates from $x_{opt} \sim 0.24$ in either direction, and the tetragonal volume fraction correspondingly diminishes, the phase separation results in small islands

of superconducting tetragonal material with a characteristic length scale embedded in a matrix of orthorhombic $\text{BaPb}_{1-x}\text{Bi}_x\text{O}_3$ that is either poorly conducting for $x < x_{opt}$ or poorly insulating for $x > x_{opt}$. This distinction has important consequences for the evolution of the superconducting properties.

The significance of the structural modulation can be readily appreciated by comparing the associated length scales of the disordered stripes, d , w and ζ (solid data points in fig. 4), with the Ginzburg-Landau coherence length, $\xi_{GL}(0)$ (blue curve in the same figure), for samples with $x < x_{opt}$, $x \approx x_{opt}$ (optimally doped), and $x > x_{opt}$, with approximate T_c values of 7K, 10.5K and 7K respectively. We estimate $\xi_{GL}(0)$ from $H_{c2}(0)$, having used the standard Werthamer-Helfand-Hohenberg approximation to determine $H_{c2}(0)$ from $H_{c2}(T)$. We employed both 50% and 90% criteria to extract $H_{c2}(T)$ from resistive transitions, leading to a narrow band of estimated values for $\xi_{GL}(0)$. Inspection of Fig. 4 reveals that the three length scales associated with the phase separation are of the same order of magnitude as the superconducting coherence length, and largely independent of Bi concentration. The shortest length scale, ζ , which characterizes the size of coherent regions within a given stripe, has a weak composition dependence, but does not grow to be larger than the superconducting coherence length for any composition, and is therefore expected to be less relevant than the larger length scales d and w associated with the period and width of the stripes. For low Bi concentrations, $x < x_{opt}$, the coherence length is larger than the width of individual stripes. However, at optimal doping, the width of individual stripes almost exactly matches the superconducting coherence length. Further increasing the Bi concentration appears to result in a saturation of $\xi_{GL}(0)$ which remains comparable to w . This behavior is highly suggestive of an important role for the nanostructure in determining the shape of the superconducting dome, as we describe below.

In the context of an electronically-inhomogeneous system, where the coulomb potential seen by electrons varies spatially in a periodic way, with characteristic length λ , it has been shown theoretically that T_c does not necessarily track the pairing scale Δ_0 , i.e. the superconducting gap magnitude [4]. Rather, the evolution of T_c is bounded above by two parameters: the pairing scale Δ_0 and the phase ordering temperature T_θ . In the limit where $\lambda \ll \xi$ (where ξ is the superconducting coherence length), $T_\theta \gg \Delta_0$, and T_c will be determined by Δ_0 . However, in the limit $\lambda \gg \xi$, the phase ordering temperature T_θ is small compared to the pairing amplitude Δ_0 , and T_c is entirely determined by T_θ , meaning that T_c is suppressed with respect to Δ_0 . In this regime the material behaves as a granular superconductor, characterized by superconducting “islands” that are only weakly coupled. For a system where the length scale of phase separation evolves with respect to the superconducting

coherence length (or vice-versa), the maximum T_c value is obtained in the crossover regime of the curves of T_θ and Δ_0 , which happens at $\lambda \sim \xi$. This regime has been dubbed “optimal inhomogeneity” [4, 25]. In the case of $\text{BaPb}_{1-x}\text{Bi}_x\text{O}_3$, the phase separation is not necessarily referring to electronic phase separation due to variations in coulomb interaction, but rather the local variation in pairing interaction of the two coexisting polymorphs, although a similar set of arguments clearly applies.

The phenomenology of $\text{BaPb}_{1-x}\text{Bi}_x\text{O}_3$ appears to be consistent with such a scenario, in which tetragonal and orthorhombic polymorphs correspond to regions of the bulk material with large and small pairing interactions respectively. The evolution with doping of the relative length scales characterized by ξ_{GL} and the phase separation is very suggestive of optimal doping being a turning point from a macroscopic inhomogeneous superconductor (with ξ_{GL} bigger than other characteristic length scales associated with disorder) for $x < x_{opt}$ to a phase-fluctuation-dominated granular superconductor for $x > x_{opt}$ (illustrated schematically in figure 1). Indeed, several signatures of granular superconductivity are observed in this regime, such as negative magnetoresistance for fields above $H_{c2}(T)$, and scaling reminiscent of a superconductor-insulator quantum phase transition [14]. Additionally, scanning tunneling spectroscopy (STS) measurements for compositions beyond optimal doping show a large variation in gap values as a function of position, with maximum values exceeding those found in the higher T_c optimally doped material [26], suggesting that samples with $x > x_{opt}$ have a larger local pairing amplitude than expected for their macroscopic T_c , and even for an 11 K superconductor. This observation is consistent with a macroscopic T_c being bounded by the phase ordering line, T_θ , i.e., with a granular superconductor picture (see figure 1). Significantly, these observations imply that for $x > x_{opt}$ the superconducting phase of this material (the tetragonal polymorph) is in fact a higher-temperature superconductor, possibly even comparable to the other bismuthate superconductor $\text{Ba}_{1-x}\text{K}_x\text{BiO}_3$ [15].

In the above analysis, the only significance of the stripe-like character of the nanostructure of $\text{BaPb}_{1-x}\text{Bi}_x\text{O}_3$ has been that it has enabled us to establish the characteristic length-scales with a little more precision than if we had assumed a more isotropic morphology. However, the stripe-like morphology possibly has a much deeper significance. In the context of $\text{BaPb}_{1-x}\text{Bi}_x\text{O}_3$, this might provide a natural means to understand the unusual scaling behavior observed at the superconductor-insulator transition close to optimal doping in this material [14, 24], motivating theoretical investigation of percolation effects near the quantum phase transition for a material with a “stripy” morphology. More broadly, several families of underdoped cuprates have been shown to exhibit stripe and/or unidirectional

CDW formation [1–3]. In the case of the cuprates, the stripe/CDW order is driven by spontaneous electronic order, whereas for the bismuthates the stripe-like nanostructure is quenched from higher temperature [27]. Significantly, in both cases, the stripe-like phase separation and superconductivity are found to have comparable length scales. In this broader context, $\text{BaPb}_{1-x}\text{Bi}_x\text{O}_3$ provides a model system to explore the effects of stripe-like phase separation on superconductivity, and in particular on the associated phenomenology of optimal inhomogeneity.

The authors thank S. A. Kivelson for helpful discussions. This work is supported by AFOSR Grant No. FA9550-09-1-0583. The electron microscopy was performed at Ames Laboratory (Y.Z. and M.J.K.) and supported by the U.S. Department of Energy (DOE), Office of Basic Energy Science (BES), Division of Materials Sciences and Engineering, under Contract No. DE-AC02-07CH11358. C.P. and H.C.M. were supported by US Department of Energy (DOE), Office of Science, Basic Energy Sciences (BES), Materials Sciences and Engineering Division, under contract DE-AC02-76SF00515.

APPENDICES

Appendix A: Glazer’s notation

The ideal cubic perovskite ABO_3 , described by the space group $Pm\bar{3}m$, can be represented as a network of corner-sharing BO_6 octahedra. ‘A’ atoms sit in the geometric center of the gap between oxygen octahedra. This structure is a “simple” and highly symmetric one; however, most materials with perovskite structures are not in their ideal cubic form, but their structure can nevertheless be represented as coming from distortions from this ideal configuration. The types of distortions found in perovskites can be narrowed down to three types: B-cation displacements within an octahedra; distortions of the BO_6 octahedral unit; and, the most common one and subject of this section, and of Glazer’s study [21], the rigid tilting of the corner-sharing BO_6 linked-octahedra units. This last type of distortion was described by Glazer in terms of tilt components along the three different pseudocubic (PC) axes, referred to the original undistorted cubic perovskite. Such pseudocubic axes coincide with the tetrad axes of the octahedra. Given the octahedra corner connections, a tilt about a pseudocubic axis determines the tilts in the directions perpendicular to this axis. However, the tilt of the successive octahedra along the same axis can be either in the same direction or in the opposite direction. With this in mind, the different possibilities of tilt-distortions can be labeled by the notation $a^*b^*c^*$, where a , b , c refer to tilts around the $[100]_{PC}$, $[010]_{PC}$ and $[001]_{PC}$ axes, respectively. If letters are repeated, the tilts are equal for their respective

axis. The superscript * can be either 0, for no-tilt along an axis; +, for tilt of successive octahedra in the same sense; or -, for tilt of successive octahedra in the opposite sense [22]. For example, the $I4/mcm$ space group is represented by the notation $a^0a^0c^-$, which means zero tilt about the $[100]_{PC}$ and $[010]_{PC}$ axes, and finite tilt about the $[001]_{PC}$ axis, with opposite rotation of the successive octahedra along this axis. The $Ibmm$ space group is represented by the notation $a^-a^-c^0$, which means equal tilts about the $[100]_{PC}$ and $[010]_{PC}$ axes (equivalent to a tilt about the $[110]_{PC}$ direction), with opposite rotation of the successive octahedra along these axes, and zero tilt about the $[001]_{PC}$ axis.

Appendix B: Electron diffraction patterns

Simulated electron diffraction patterns for tetragonal $I4/mcm$ and orthorhombic $Ibmm$ polymorphs of $BaPb_{1-x}Bi_xO_3$ along the $[001]_T$ and $[010]_T$ zone axis were obtained through the University of Illinois web-based electron microscopy application software (WEB-EMAPS) [28], using the atomic parameters shown in tables I and II. Along both of these zone axis, the (hkl) set of reflections with hkl even, are common to both, orthorhombic and tetragonal phases. However, for both zone axes, the (hkl) set of reflections with hkl odd, appears only in the orthorhombic phase and not in the tetragonal. In ref. 14 we showed that it is possible to recreate the spatial separation of the two polymorphs by systematically masking these diffraction peaks and performing an inverse Fourier transform (IFFT). The result of applying a mask such that only the even (hkl) peaks, common to both the tetragonal and orthorhombic phases, show an ordered array of planes of atoms (see figure 6 in ref. 14). In contrast, the result of applying a mask to the $[101]_T/[110]_T$ peaks, attributed only to the $Ibmm$ orthorhombic phase, reveals a spatial variation due to the densely intergrown nanostructure, as shown in Fig. 3 of the main manuscript, and Figs. A3, A4 and A5 of this supplemental material.

Atom	Wyck.	Site	x/a	y/b	z/c
Ba	4b	-42m	0	0.5	0.25
Pb/Bi	4c	4/m	0	0	0
O1	8h	m.2m	0.2179(14)	0.7179(14)	0
O2	4a	422	0	0	0.25

TABLE I: Atomic parameters for tetragonal $BaPb_{1-x}Bi_xO_3$ (space group $I4/mcm$, No. 140), with $x \approx 0.28$, as reported in ref. 7. The site 4c is fully occupied by Pb/Bi, and the Pb to Bi ratio is determined by x .

Atom	Wyck.	Site	x/a	y/b	z/c
Ba	4e	mm2	0.496	0	0.25
Pb/Bi	4a	2/m	0	0	0
O1	4e	mm2	0.0496	0	0.25
O2	8g	.2	0.25	0.25	0.9741

TABLE II: Atomic parameters for orthorhombic $BaPb_{1-x}Bi_xO_3$ (space group $Ibmm$, No. 74), with $x \approx 0.28$, as reported in ref. 7. The site 4a is fully occupied by Pb/Bi, and the Pb to Bi ratio is determined by x .

Appendix C: Definition of the correlation function

The spatial autocorrelation function $G(\vec{r})$ of an image is defined as the statistical correlation of two points separated by a vector $\vec{r} = \vec{r}_i - \vec{r}_j$, where \vec{r}_i and \vec{r}_j are the positions of those two points in the image [29].

$$G(\vec{r}) = \frac{1}{N(\vec{r})} \sum_{i,j} \frac{(I_i - \langle I \rangle_1)(I_j - \langle I \rangle_2)}{\sigma_1 \sigma_2} \quad (C1)$$

where

$$N(\vec{r}) = \sum_{i,j} \delta_{\vec{r},(\vec{R}_i - \vec{R}_j)} \quad (C2a)$$

$$\langle I \rangle_1 = \frac{1}{N(\vec{r})} \sum_{i,j} \delta_{\vec{r},(\vec{R}_i - \vec{R}_j)} I_i \quad (C2b)$$

$$\langle I \rangle_2 = \frac{1}{N(\vec{r})} \sum_{i,j} \delta_{\vec{r},(\vec{R}_i - \vec{R}_j)} I_j \quad (C2c)$$

$$\sigma_1^2 = \left(\frac{1}{N(\vec{r})} \sum_{i,j} \delta_{\vec{r},(\vec{R}_i - \vec{R}_j)} I_i^2 \right) - (\langle I \rangle_1)^2 \quad (C2d)$$

$$\sigma_2^2 = \left(\frac{1}{N(\vec{r})} \sum_{i,j} \delta_{\vec{r},(\vec{R}_i - \vec{R}_j)} I_j^2 \right) - (\langle I \rangle_2)^2 \quad (C2e)$$

The average spatial autocorrelation function $\langle G(\vec{r}) \rangle$ is the result of averaging the correlation function of all vectors with the same magnitude $|\vec{r}|$. The angle-dependent autocorrelation function $\langle G_\theta(\vec{r}) \rangle$ is the result of averaging the correlation function of all vectors with orientation θ with respect to the horizontal axis, and magnitude $|\vec{r}|$.

Appendix D: Correlation function for reduced-resolution images

Fig. A1(a) shows a $19 \times 19 \text{ nm}^2$ portion of the $[110]_T$ filtered IFFT of the HRTEM image in fig. 2(b) of the main manuscript. This image keeps the information of both the atomic periodicity as well as a larger-scale contrast

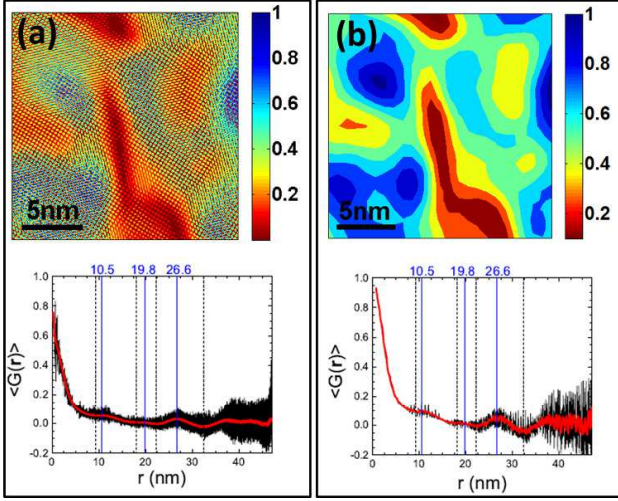


FIG. A1: (Color online) (a) $19 \times 19 \text{ nm}^2$ portion of a $[110]_T$ filtered-and-reconstructed HRTEM image for a sample with bismuth concentration of $x=0.18$, and its corresponding correlation function below it, showing the atomic resolution detail. (b) Same image as in (a), and its corresponding correlation function, after a $7.5 \text{ \AA} \times 7.5 \text{ \AA}$ averaging, eliminating the atomic resolution information while maintaining the broader orthorhombic structural variation. The red curves in the correlation functions are 3nm smoothing of the original black curves.

variation, reflecting variations in the local “orthorhombicity” across the sample. The image in figure A1(b) is the result of a resolution reduction by adjacent averaging, of the image in fig. A1(a), from 0.47 \AA per pixel, to 7.5 \AA per pixel, therefore eliminating the atomic resolution information while keeping the longer-range variation in “orthorhombicity”. The bottom parts of fig. A1(a) and A1(b) show the computed average spatial correlation functions of their respective images on top. The vertical lines in $\langle G(\vec{r}) \rangle$ label local minima and maxima positions $|\vec{r}|$, being equivalent for both, the original resolution image in fig. A1(a), and the reduced resolution image in fig. A1(b). For the purpose of our analysis, we consider only the reduced resolution images, given that these conserve the information of the longer-scale structural variation while reducing the computational requirements.

Appendix E: Correlation function for a stripe model

The angular dependent correlation function $\langle G_\theta(\vec{r}) \rangle$ was computed for an image of size 128×128 pixels, showing perfect stripes formation, with stripes of width $w = 15$ pixels and periodicity $d = 30$ pixels, running along an angle $\alpha = 90^\circ$ with respect to the horizontal axis (fig. A2(a)). The color scale of the right hand side plot of fig.

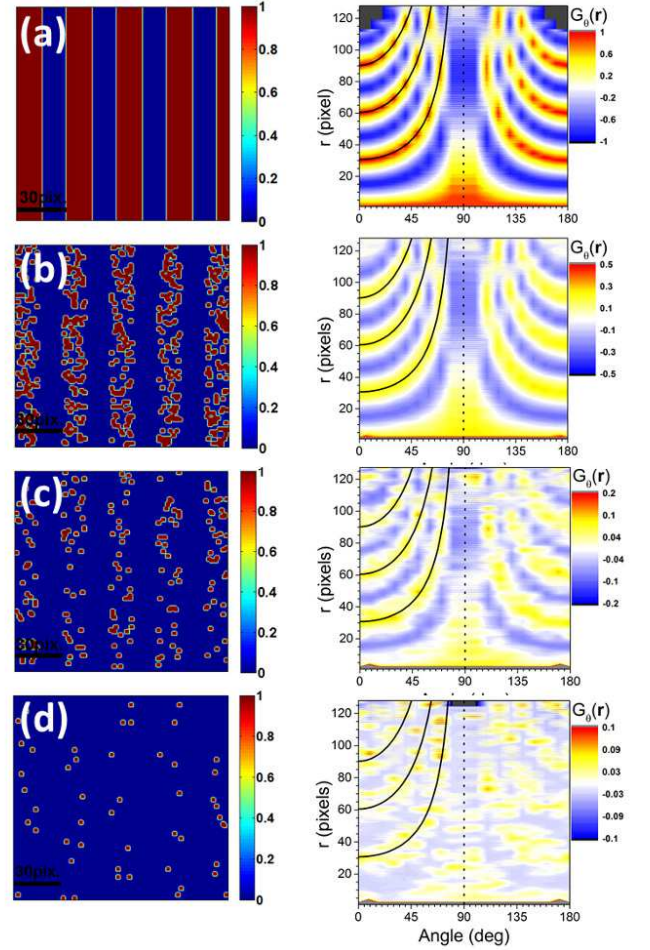


FIG. A2: (Color online) Images of 128×128 pixels, with stripes of width $w = 15$ pixels, separated between them by $d = 30$ pixels. For the different images, a broken-up character of a different level was introduced, as a number of islands of size 3×3 pixels, placed at random positions within the red stripes. The number of islands within a stripe for each image is: (a) Infinite (perfect stripe formation), (b) 120 islands, (c) 40 islands, (d) 10 islands. For each image, the angle-dependent correlation function $\langle G_\theta(\vec{r}) \rangle$ is shown in the right-hand panel. Black lines in these plots follow the functional form $N * d / \cos((\alpha - 90^\circ) - \theta)$, where $N = 1, 2, 3, \dots$, $d = 30$ and $\alpha = 90$.

A2(a) represents the value of $\langle G_\theta(\vec{r}) \rangle$, as a function of the angle θ with the horizontal axis and the magnitude of \vec{r} . Maxima of $\langle G_\theta(\vec{r}) \rangle$ for this image appear along following the functional form $N * d / \cos((\alpha - 90^\circ) - \theta)$ (shown by the black solid lines), where $N = 1, 2, 3, \dots$. Figures A2(b)-(d) show images of the same size and with stripes of the same width and periodicity as in (a), but where a progressively broken-up character has been introduced for each image. For these images, the maxima of $\langle G_\theta(\vec{r}) \rangle$ follow in average the same functional form as the orig-

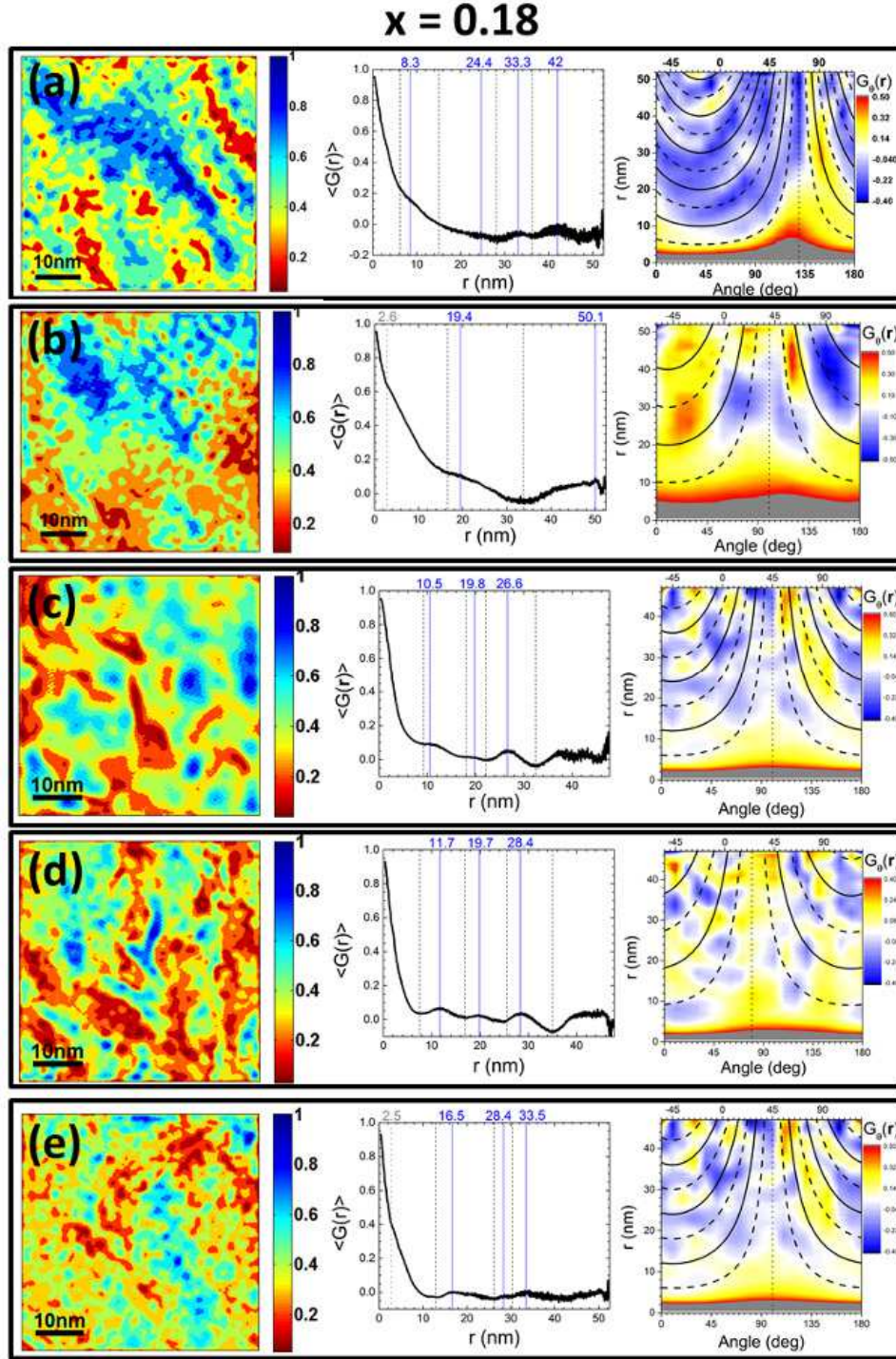


FIG. A3: (Color online) $[110]_T/[101]_T$ filtered-and-reconstructed HRTEM images (first-column figures), for different samples with bismuth concentration of $x=0.18$. For each horizontal panel, the center column shows the corresponding average spatial correlation function, $\langle G(\vec{r}) \rangle$. Solid blue vertical lines indicate the local maxima in $\langle G(\vec{r}) \rangle$, while dashed-black vertical lines indicate local minima. The third column in each horizontal panel shows the angle-dependent spatial correlation function, $\langle G_\theta(\vec{r}) \rangle$ on a color scale, as a function of $|\vec{r}|$ (vertical axis) and the angle θ with the horizontal (bottom-axis) or the $[200]_T$ crystalline axis (top-axis). Solid and dashed lines represent the best fits to $N \times d / \cos((\alpha - 90^\circ) - \theta)$ and $(2N - 1) \times w / \cos((\alpha - 90^\circ) - \theta)$ for the local maxima and minima respectively.

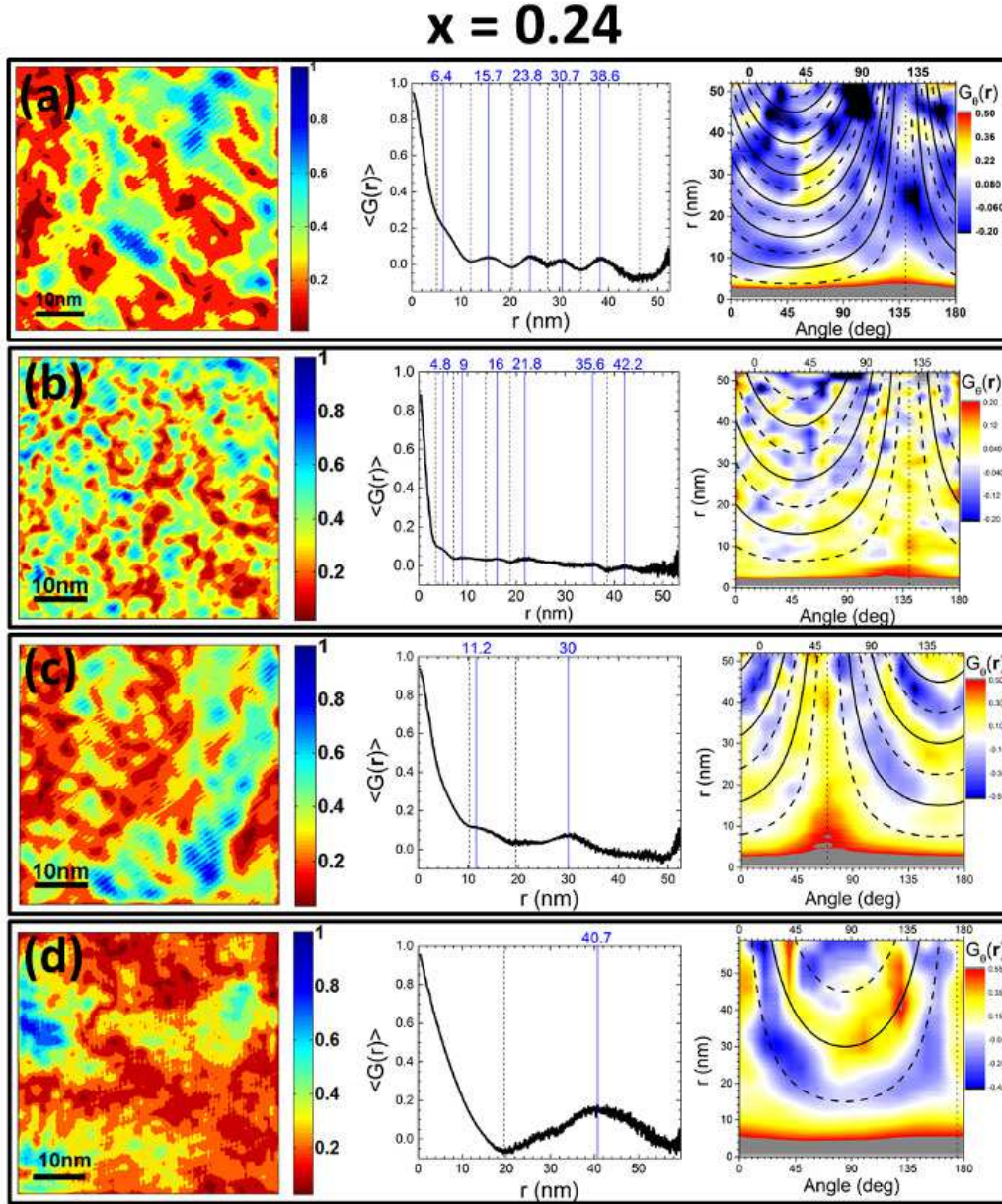


FIG. A4: (Color online) $[110]_T/[101]_T$ filtered-and-reconstructed HRTEM images (first-column figures), for different samples with bismuth concentration of $x=0.24$. For each horizontal panel, the center column shows the corresponding average spatial correlation function, $\langle G(\vec{r}) \rangle$. Solid blue vertical lines indicate the local maxima in $\langle G(\vec{r}) \rangle$, while dashed-black vertical lines indicate local minima. The third column in each horizontal panel shows the angle-dependent spatial correlation function, $\langle G_\theta(\vec{r}) \rangle$ on a color scale, as a function of $|\vec{r}|$ (vertical axis) and the angle θ with the horizontal (bottom-axis) or the $[200]_T$ crystalline axis (top-axis). Solid and dashed lines represent the best fits to $N \times d / \cos((\alpha - 90^\circ) - \theta)$ and $(2N - 1) \times w / \cos((\alpha - 90^\circ) - \theta)$ for the local maxima and minima respectively.

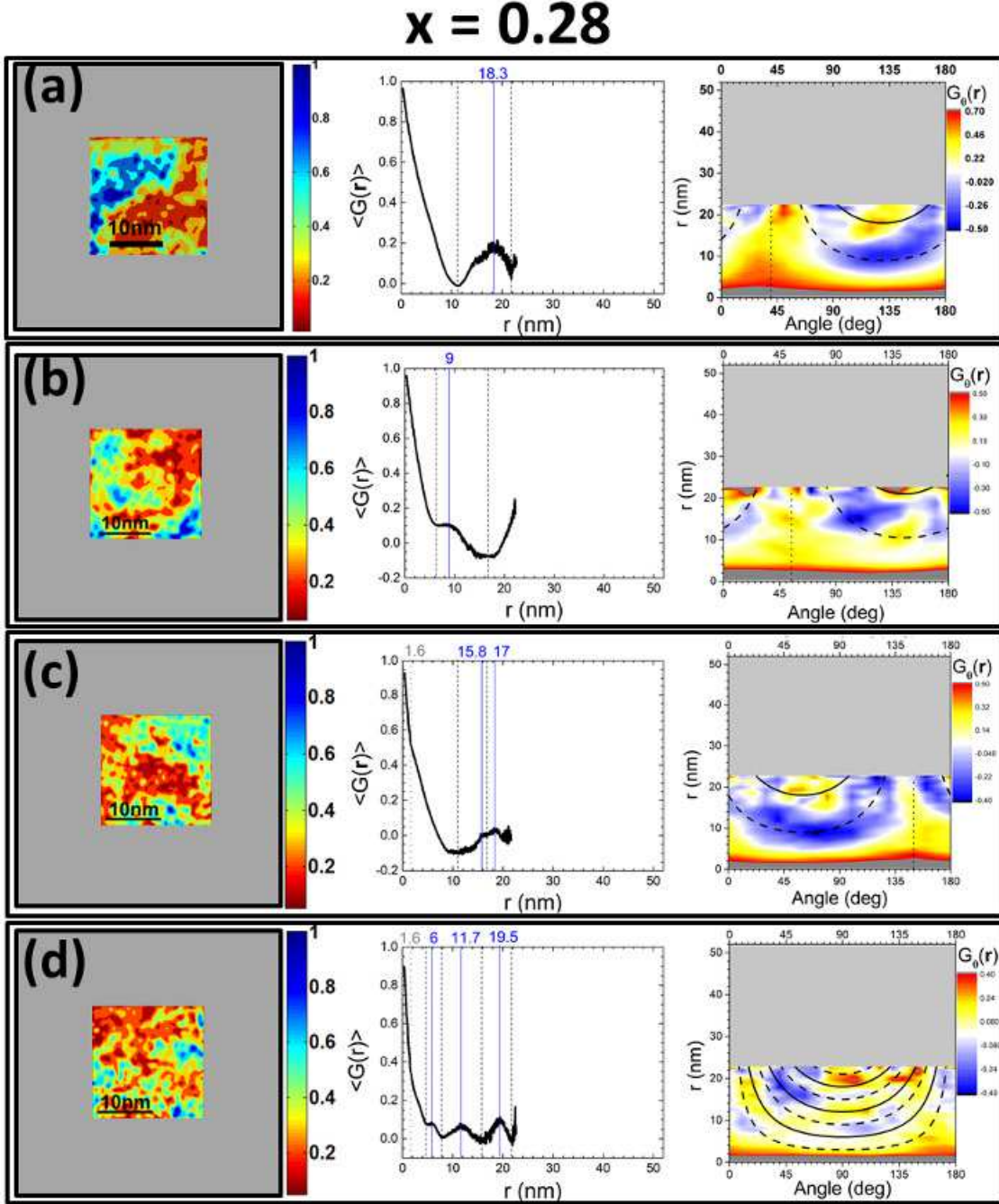


FIG. A5: (Color online) $[110]_T/[101]_T$ filtered-and-reconstructed HRTEM images (first-column figures), for different samples with bismuth concentration of $x=0.28$. These images were taken for a smaller area than the ones for the $x = 0.18$ and $x = 0.24$ samples. To preserve a direct comparison with those data, the images are shown on the same scale as for figs. A3 and A4. For each horizontal panel, the center column shows the corresponding average spatial correlation function, $\langle G(\vec{r}) \rangle$. Solid blue vertical lines indicate the local maxima in $\langle G(\vec{r}) \rangle$, while dashed-black vertical lines indicate local minima. The third column in each horizontal panel shows the angle-dependent spatial correlation function, $\langle G_\theta(\vec{r}) \rangle$ on a color scale, as a function of $|\vec{r}|$ (vertical axis) and the angle θ with the horizontal (bottom-axis) or the $[200]_T$ crystalline axis (top-axis). Solid and dashed lines represent the best fits to $N \times d / \cos((\alpha - 90^\circ) - \theta)$ and $(2N - 1) \times w / \cos((\alpha - 90^\circ) - \theta)$ for the local maxima and minima respectively.

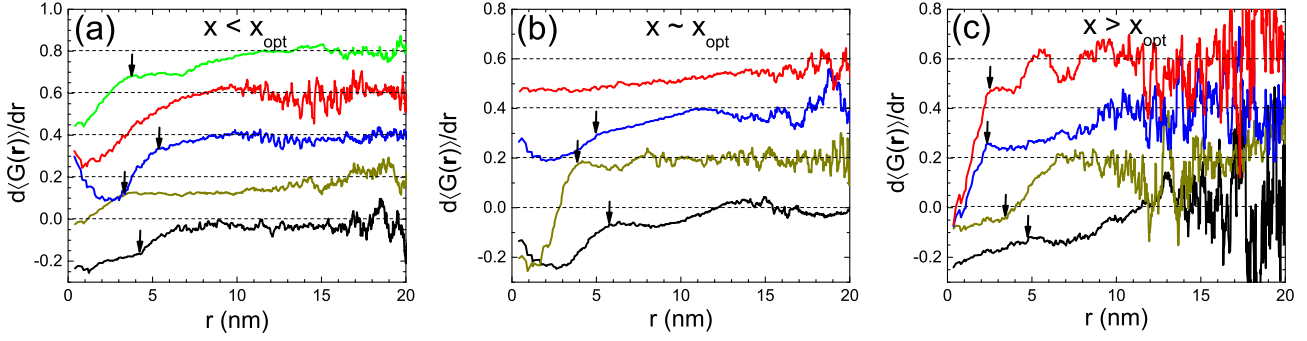


FIG. A6: (Color online) Derivative of the average correlation function $\langle G(\vec{r}) \rangle$ (for the low- r tail region) of different filtered-and-reconstructed images of samples with Bi concentrations of (a) $x = 0.18$ ($x < x_{opt}$), (b) $x = 0.24$ ($x \approx x_{opt}$) and (c) $x = 0.28$ ($x > x_{opt}$). Dashed horizontal lines mark the $d\langle G(\vec{r}) \rangle/dr = 0$ zone for each curve. Arrows mark the points determining the disorder length-scale within a stripe, ζ . Average values of ζ are shown in Fig. 4 of the main manuscript, as a function of x .

inal zero-disorder stripe model, but the local maximum value of $\langle G_\theta(\vec{r}) \rangle$ progressively decreases in value, from 1 for the perfect-stripes image in fig. A2(a), to about 0.1 for the most broken-up image in fig. A2(d). At the same time, the arcs where the maximum values of $\langle G_\theta(\vec{r}) \rangle$ appear get progressively more broken-up, although its average functional form is preserved, and its periodicity can be well identified. The angle dependent correlation functions $\langle G_\theta(\vec{r}) \rangle$ observed in the $[110]_T/[101]_T$ filtered-and-reconstructed images analyzed throughout this article show very similar features to the ones observed in this model of broken-up stripes.

Appendix F: Correlation function for all the images studied

Figures A3, A4 and A5 of this supplemental material show $[110]_T/[101]_T$ filtered-and-reconstructed images (left-hand panels) for a total of five $x = 0.18$ samples (fig. A3), four $x = 0.24$ samples (fig. A4) and four $x = 0.28$ samples (fig. A5), as well as their respective average spatial correlation function $\langle G(\vec{r}) \rangle$ (central panels) and angle-dependent spatial correlation function $\langle G_\theta(\vec{r}) \rangle$ (right-hand panels). The first image of each figure had been already shown in figure 3 of the main manuscript; however it is shown again for completeness and with the spirit of presenting the average correlation function that was not presented before. The characteristic length scales of phase separation shown in figure 4 of the main manuscript are: (1) stripes periodicity, d , (2) stripes width, w , and (3) the correlation length within a single stripe, ζ . These length scales were determined for all of the figures, and the average value for each quantity determined and plotted as a function of Bi concentration in Fig. 4 of the main manuscript.

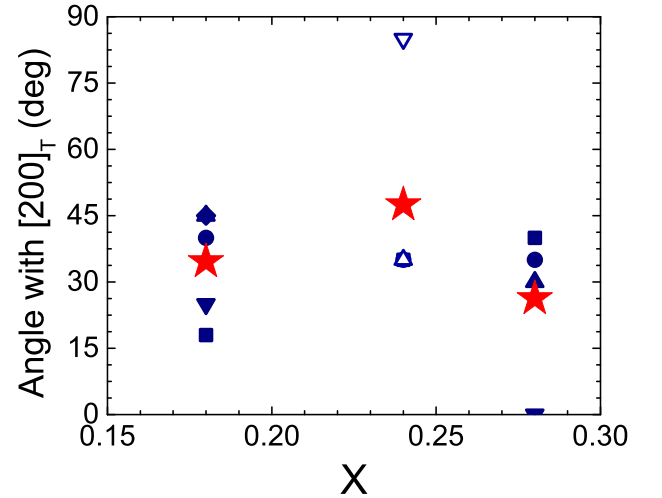


FIG. A7: (Color online) Orientation of stripes with respect to the $\{200\}_T$ crystalline axis as a function of Bi concentration, for all the samples studied. Open blue symbols show the orientation for samples with images taken along the $[001]_T$ zone axis; full blue symbols show the orientation for samples with images taken along the $[010]_T$ zone axis. Star-shape full red symbols show the average orientation for each composition.

Appendix G: Derivative of the average correlation functions

The length-scale representing the disorder within a stripe, denoted as ζ , is picked-up more clearly in the average correlation function $\langle G(\vec{r}) \rangle$, as a kink or change of slope in the low- r tail region. This kink is more precisely seen in the derivative of this quantity, as shown in figure A6(a,b,c) for the different Bi compositions and samples of each compositions studied. Black arrows in these plots

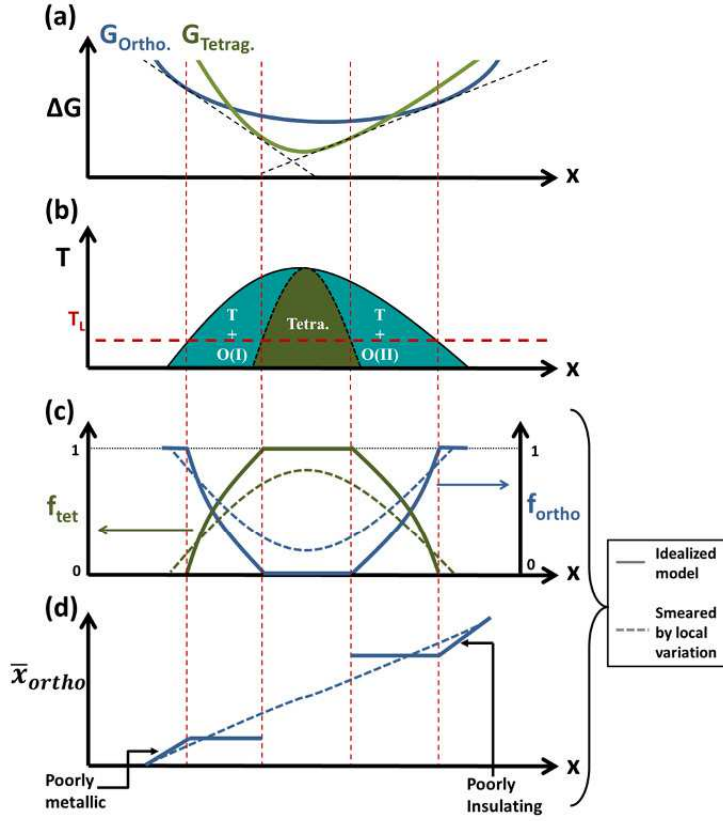


FIG. A8: (Color online) (a) Schematic diagram of the Gibbs free energy of orthorhombic ($G_{ortho.}$) and tetragonal ($G_{tetrag.}$) phases as a function of composition at a given low temperature $T = T_L$. (b) The corresponding phase diagram, showing regions of phase coexistence. At $x = x_{opt}$ the tetragonal fraction is maximum. For $x < x_{opt}$ the orthorhombic phase is labeled as O(I), and it is a low-Bi phase, presumably metallic. For $x > x_{opt}$ the orthorhombic phase is labeled O(II), and it is a rich-Bi phase, presumably insulating.

(c) Fraction of tetragonal (f_{tet} , left-axis) and orthorhombic (f_{ortho} , right-axis) phases as a function of composition, at temperature $T = T_L$ (marked by the red horizontal line in panel (b)). (d) Spatial average of orthorhombic composition, \bar{x}_{ortho} , as a function of composition, for the same temperature $T = T_L$. Solid lines in panels (c) and (d) show the evolution of these quantities with composition for the ideal case depicted in (a), whereas dashed-curves show the evolution for the case where the local free energy is modified by local strain, giving rise to a distribution of free energies that smear the otherwise sharp distinctions and features of the tetragonal and orthorhombic fractions, and spatial average of orthorhombic composition.

show the points determining the value of ζ for each sample. The average value of ζ is plotted in figure 4 of the main manuscript, together with the other length scales

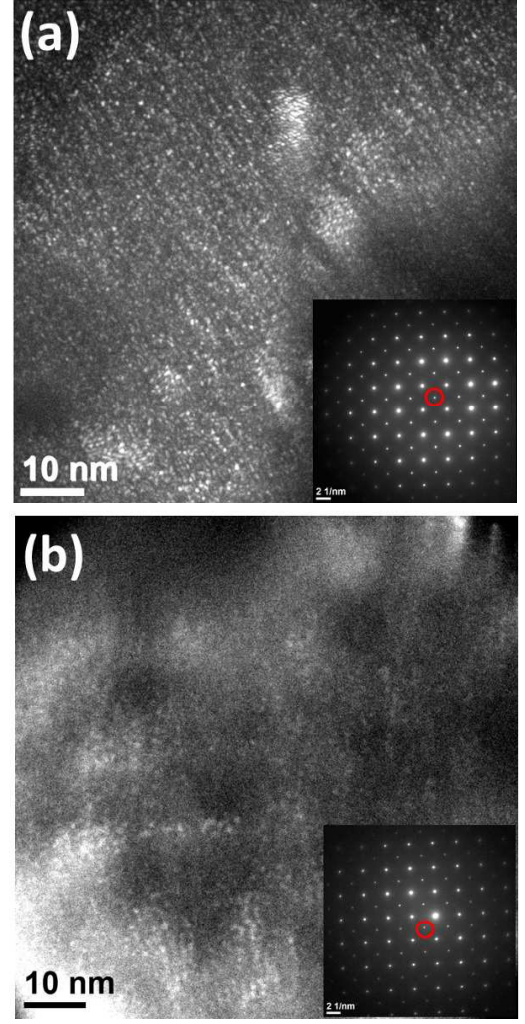


FIG. A9: (Color online) $80.8 \times 80.8 \text{ nm}^2$ dark-field TEM images, as looking down the $[001]_T$ zone axis, obtained using the (110) reflection (shown in red in the insets to both figures) for samples with Bi concentration of (a) $x = 0.18$ and (b) $x = 0.28$.

of phase separation.

Appendix H: Orientation of stripes

Fig. A7 shows the orientation of stripes with respect to the $[200]_T$ axis, for all the different samples studied, as a function of Bi concentration. The uncertainty of this measure is large given the imperfect character of the stripe patterns, however, it can be observed that the average value is close to 30° from the $\{200\}_T$ axis ($29^\circ \pm 22^\circ$).

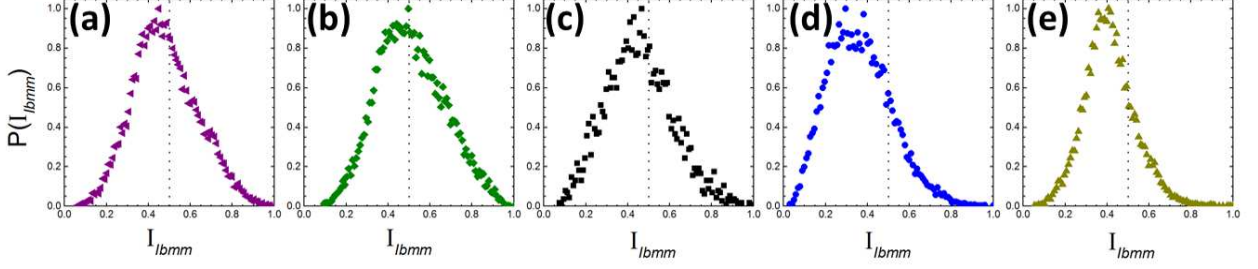


FIG. A10: (Color online) Probability distribution of orthorhombicity, $P(I_{l bmm})$, as a function of the orthorhombicity intensity, $I_{l bmm}$, for their corresponding images in figure A3 (with Bi composition of $x = 0.18$).

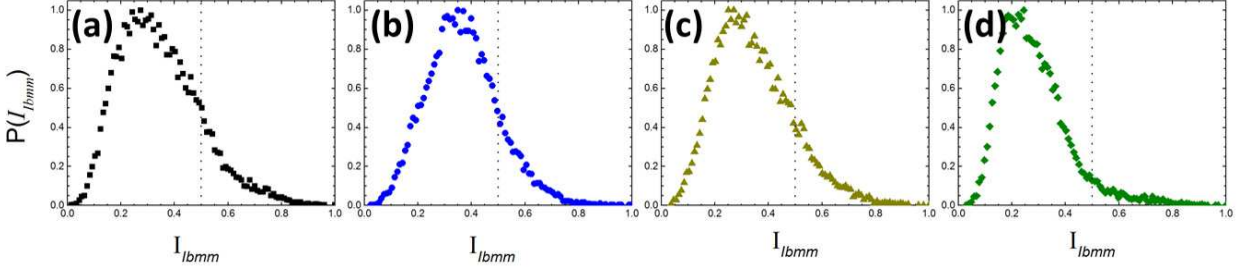


FIG. A11: (Color online) Probability distribution of orthorhombicity, $P(I_{l bmm})$, as a function of the orthorhombicity intensity, $I_{l bmm}$, for their corresponding images in figure A4 (with Bi composition of $x = 0.24$).

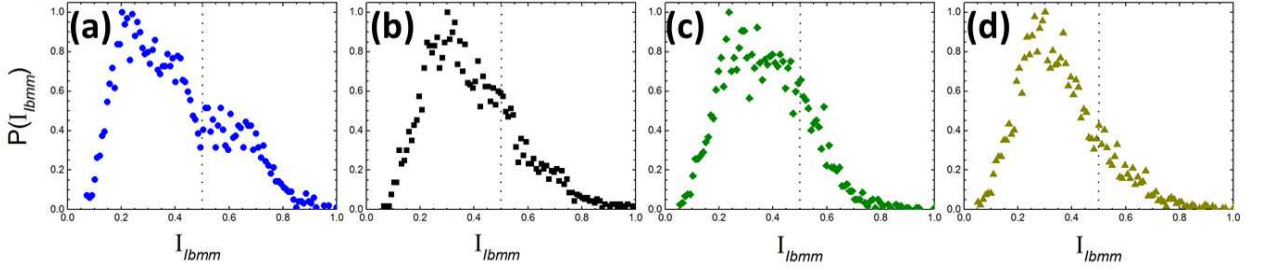


FIG. A12: (Color online) Probability distribution of orthorhombicity, $P(I_{l bmm})$, as a function of the orthorhombicity intensity, $I_{l bmm}$, for their corresponding images in figure A5 (with Bi composition of $x = 0.28$).

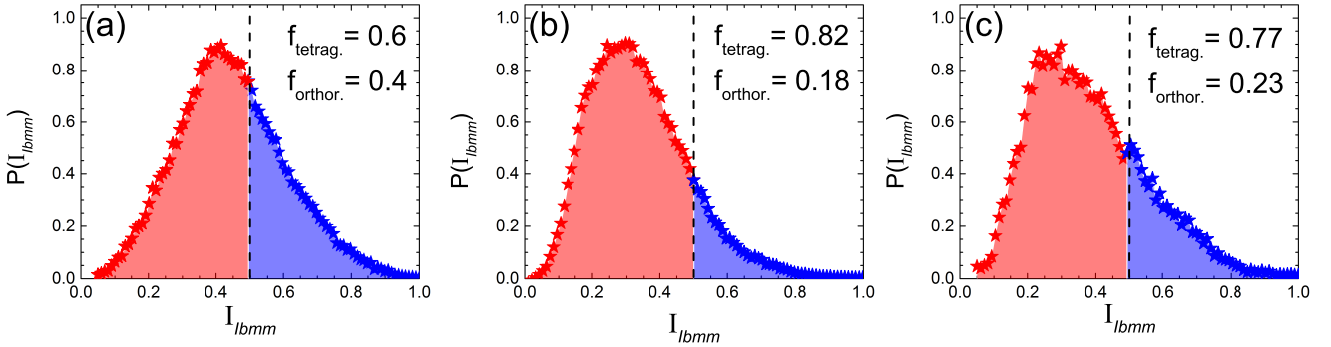


FIG. A13: (Color online) Average Probability distribution of orthorhombicity for samples with Bismuth concentration of (a) $x = 0.18$, (b) $x = 0.24$ and (c) $x = 0.28$. The blue and red shadowed regions separate the areas above and below half the intensity, from which the orthorhombic and tetragonal filling fractions can be estimated.

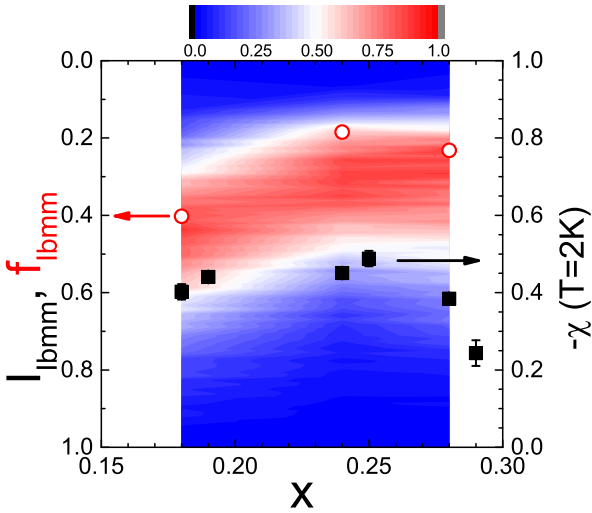


FIG. A14: (Color online) The color scale represents the probability distribution of orthorhombicity, as a function of the orthorhombicity intensity (left scale) and Bi concentration (bottom scale). The red-open circles represent the orthorhombic filling fraction f_{Ibmm} (left scale), calculated from integration of the probability distributions, with a 0.5 criteria. Black squares represent the superconducting volume fraction (right scale) determined from magnetic susceptibility measurements.

Appendix I: Phase separation model

The phase separation of tetragonal and orthorhombic polymorphs in $\text{BaPb}_{1-x}\text{Bi}_x\text{O}_3$ is presumably driven by changes in the relative Gibbs free energy of the two phases, both as a function of temperature and composition [30]. Such a scenario is illustrated schematically in fig. A8. The resulting morphology is reminiscent of spinodal decomposition, but the physical origin is somewhat different in this case, involving two competing phases. The point where the maximum tetragonal fraction is found, which for the case of $\text{BaPb}_{1-x}\text{Bi}_x\text{O}_3$ is coincident with optimal doping, $x_{opt} \approx 0.24$, demarks a separatrix between a low-Bi orthorhombic phase, O(I), for compositions $x < x_{opt}$, and a Bi-rich orthorhombic phase, O(II), for compositions $x > x_{opt}$. It has been previously shown for various metallic precipitates embedded in metallic matrices (Cu-in-Al, Ag-in-Cu, Ag-in-Al, among others) that inhomogeneous strain can cause local variations in the free-energy, modifying phase equilibria [23]. Therefore, it is reasonable to anticipate that the sharp distinctions in composition between the O(I) and O(II) phases will be blurred in practice (see panels (c) and (d) of figure A8). The resulting continuous variation in composition, and presumably lattice parameter, is consistent with results of recent x-ray and neutron diffraction mea-

surements [7]. Consequently, the resistivity of the orthorhombic matrix in which the tetragonal polymorph resides, evolves continuously from that of a poor metal to a poor insulator.

Appendix J: Dark-field TEM images

In addition to the HRTEM images used in the analysis presented throughout this work, dark-field (DF) TEM images were also taken. These images also reveal the presence of broken-up stripes, with length scales consistent with the ones obtained through the $[110]_T/[101]_T$ filtered-and-reconstructed HRTEM images analysis described in the main text. Fig. A9(a,b) shows DF images for samples with Bi concentration of $x = 0.18$ and 0.28 , respectively, along the $[001]_T$ zone axis. These DF images were obtained using the (110) reflection shown in the red circle in the insets to fig. A9(a,b). For both figures the size and distribution of the bright regions, imaged using reflection limited to the $Ibmm$ phase, mimics the small patchwork of coherent domains seen in the Fourier-filtered reconstruction. A stripy pattern, containing patches of 5-10nm, which for image in fig. A9(a) is more scattered throughout, is better seen in the image in fig. A9(b), and the length-scales observed are consistent with the ones found with the Fourier-filtered reconstruction. Note that only one of the four (110) reflections are used in the DF image, while Fourier-filtered reconstruction uses all of the $[110]$ reflections in the reconstruction. This is most likely the cause of the $(\bar{1}10)$ directionality seen in the image in figure A9(a).

Appendix K: Intensity probability distributions

We also computed the probability distribution of intensities of the $[101]_T/[110]_T$ filtered-and-reconstructed HRTEM images shown in Fig. 3 of the main text, and in Figs. A3, A4 and A5 of this document. For each image, the intensity in each pixel, which might be labelled the intensity of “orthorhombicity”, was normalized by the maximum intensity in the image, so that for all of the images this quantity goes from 0 to 1. Then, we computed the histogram of intensity, dividing the range of intensity into 100 sections. The vertical scale (counts) of each histogram is then normalized, so that for all the images this scale goes from 0 to 1. These curves are proportional to the probability distribution of intensity. The results for each image studied in this work are shown in fig. A10 for samples with Bi concentration $x = 0.18$, in fig. A11 for samples with $x = 0.24$, and in fig. A12 for samples with $x = 0.28$. For each composition, all the normalized histograms were averaged, and the result of this averaging is shown in fig. A13. From these averaged histograms we estimated the orthorhombic filling fraction,

$f_{I_{bmm}}$, as the normalized-integrated area above half the total intensity (as shown in the blue-shadowed areas in fig. A13).

The evolution of the orthorhombic volume fraction as a function of Bi concentration can be better visualized in fig. A14. The left axis of this figure shows an inverted scale (from 1 to 0) of the orthorhombic intensity. The colors in the contour plot represent values of the probability of “orthorhombicity”, i.e., the y scale in the averaged histograms shown in fig. A13, as a function of orthorhombic intensity and Bi concentration. From this figure we can observe that the maximum of the probability distribution of “orthorhombicity” (red colors) is shifted toward lower values of orthorhombicity for optimal doping, compared to samples with lower and higher Bi concentrations. As a consequence, if we represent the orthorhombic volume fraction $f_{I_{bmm}}$ as the normalized-integrated area above half the total intensity, it is minimum at optimal doping, which means that the tetragonal fraction, $f_{I_{4/mcm}} = 1 - f_{I_{bmm}}$ is maximum at this composition, with a value of 0.82 ± 0.08 . The evolution of the inverse of the orthorhombic fraction, i.e., the tetragonal fraction, approximately tracks the evolution of the superconducting volume fraction, shown in the right scale and as black squares. These observations are consistent with results from x-ray and neutron diffraction experiments by E. Climent-Pascual *et al.*[7] in polycrystalline samples, and suggest a direct connection between the tetragonal distortion and superconductivity.

-
- [1] J. M. Tranquada, B. J. Sternlieb, J. D. Axe, Y. Nakamura, and S. Uchida, *Nature* **375**, 561 (1995).
- [2] C. Howald, H. Eisaki, N. Kaneko, M. Greven, and A. Kapitulnik, *Phys. Rev. B* **67**, 014533 (2003).
- [3] M. L. Tacon, A. Bosak, S. M. Souliou, G. Dellea, T. Loew, R. Heid, K.-P. Bohnen, G. Ghiringhelli, M. Krisch, and B. Keimer, *Nature Phys.* **10**, 52 (2014).
- [4] S. A. Kivelson and E. Fradkin, *Treatise of High Temperature Superconductivity: Chapter 15* (Springer, 2007).
- [5] S. A. Kivelson, I. P. Bindloss, E. Fradkin, V. Oganessian, J. M. Tranquada, A. Kapitulnik, and C. Howald, *Rev. Mod. Phys.* **75**, 1201 (2003).
- [6] E. Berg, D. Orgad, and S. A. Kivelson, *Phys. Rev. B* **78**, 094509 (2008).
- [7] E. Climent-Pascual, N. Ni, S. Jia, Q. Huang, and R. J. Cava, *Phys. Rev. B* **83**, 174512 (2011).
- [8] S. Uchida, K. Kitazawa, and S. Tanaka, *Phase Transitions* **8**, 95 (1987).
- [9] A. Taraphder *et al.*, *International J. of Mod. Phys. B* **10**, 863 (1996).
- [10] A. M. Gabovich and D. P. Moiseev, *Sov. Phys. Usp.* **29**, 1135 (1986).
- [11] B. A. Baumert, *J. Supercond.* **8**, 175 (1995).
- [12] R. J. Cava *et al.*, *Nature* **332**, 814 (1988).
- [13] A. W. Sleight, J. L. Gillson, and P. E. Bierstedt, *Solid State Commun.* **17**, 27 (1975).
- [14] P. Giraldo-Gallo, H.-O. Lee, Y. Zhang, M. J. Kramer, M. R. Beasley, T. H. Geballe, and I. R. Fisher, *Phys. Rev. B* **85**, 174503 (2012).
- [15] K. Luna, P. Giraldo-Gallo, T. H. Geballe, I. R. Fisher, and M. R. Beasley, *Arxiv: 1311.4212v1* (2013).
- [16] L. F. Mattheiss and D. R. Hamann, *Phys. Rev. B* **28**, 4227 (1983).
- [17] C. M. Varma, *Phys. Rev. Lett.* **61**, 2713 (1988).
- [18] Z. P. Yin, A. Kutepov, and G. Kotliar, *Phys. Rev. X* **3**, 021011 (2013).
- [19] D. T. Marx, P. G. Radaelli, J. D. Jorgensen, R. L. Hitterman, D. G. Hinks, S. Pei, and B. Dabrowski, *Phys. Rev. B* **46**, 114 (1992).
- [20] J. B. Boyce, F. G. Bridges, T. Claeson, T. H. Geballe, G. G. Li, and A. W. Sleight, *Phys. Rev. B* **46**, 114 (1992).
- [21] A. M. Glazer, *Acta Cryst.* **B28**, 3384 (1972).
- [22] C. J. Howard and H. T. Stokes, *Acta Cryst.* **B54**, 782 (1998).
- [23] J. K. Lee, D. M. Barnett, and H. I. Aaronson, *Metallurgical Transactions A* **8**, 963 (1977).
- [24] P. Giraldo-Gallo, H.-O. Lee, M. R. Beasley, T. H. Geballe, and I. R. Fisher, *J. Supercond. and Nov. Magn.* **26**, 2675 (2013).
- [25] E. Arrigoni and S. A. Kivelson, *Phys. Rev. B* **68**, 180503 (2003).
- [26] C. Parra, F. C. Niestemski, A. W. Contryman, P. Giraldo-Gallo, T. H. Geballe, I. R. Fisher, and H. C. Manoharan, To be published (2014).
- [27] R. J. Cava, private communication (2012).
- [28] J. Zuo and J. C. Mabon, “Web-based electron microscopy application software: Web-emaps.” University of Illinois. <http://emaps.mrl.uiuc.edu>. (1992).
- [29] M. Fratini, N. Poccia, A. Ricci, G. Campi, M. Burghammer, G. Aeppli, and A. Bianconi, *Nature* **466**, 841 (2010).
- [30] I. R. Fisher, M. C. Shapiro, and J. G. Analytis, *Philosophical Magazine* **92**, 19 (2012).